RELATION BETWEEN COOL AND HOT POST-FLARE LOOPS OF 26 JUNE 1992 DERIVED FROM OPTICAL AND X-RAY (SXT-YOHKOH) OBSERVATIONS

B. SCHMIEDER
Observatoire de Meudon, DASOP, F-92195 Meudon Cedex, France

P. HEINZEL
Astronomical Institute, CZ-25165 Ondřejov, Czech Republic

J.E. WIIK
ESA Space Science Department, ESTEC Postbus 299, NL-2200 AG Noordwijk, The Netherlands

J. LEMEN
Lockheed Palo Alto Research Laboratory, Palo Alto, USA

B. ANWAR
Ionospheric R and D Center, Lapan, Jl.Dr Junjuan 133 Bandung 40173, Indonesia

P. KOTRČ
Astronomical Institute, CZ-25165 Ondřejov, Czech Republic

and

E. HIEI
Meisei University, NAO, 2-1-1, Hodokubo, Hino, 191 Tokyo, Japan

(Received 18 November, 1994)

Abstract. We have analyzed the physical conditions of the plasma in post-flare loops with special emphasis on dynamics and energy transport using SXT-data (hot plasma) and optical ground-based data from Pic du Midi, Wrocław, and Ondřejov (cool plasma). By combining the Hα observations with the SXT images we can understand the relationship between cool and hot plasmas, the process of cooling post-flare loops and the mechanism which maintains the long duration of these loops. Using recent results of NLTE modeling of prominence-like plasmas, we derive the emission measure of cool Hα loops and this gives us a realistic estimate of the electron density (2.2×10^{10} cm $^{-3}$). Then, by comparing this emission measure with that of hot loops derived from SXT data, we are able to estimate the ratio between electron densities in hot and cool loops taking into account the effect of geometrical filling factors. This leads to the electron density in hot loops 7×10^9 cm^{-3}. We also derive the temperature of hot X-ray loops ($\simeq 5.5 \times 10^6$ K), which, together with the electron density, provides the initial values for solving the time-dependent energy balance equation. We obtain the cooling times which are compared to a typical growth-time of the whole loop system ($\sim$ 2000 s). In the legs of cool Hα loops, we observe an excess of the emission measure which we attribute to the effect of Doppler brightening (due to large downflow velocities).

1. Introduction

Since the discovery of large systems of loops appearing after the impulsive phase of solar flares, so-called post-flare loops, a great amount of observations has been collected (see reviews of Švestka, 1989; Švestka and Cliver, 1992; Schmieder,

Solar Physics **156:** 337–361, 1995.

1992; and book of Bray *et al.,* 1991). Few minutes after the occurence of two-ribbon flares dense cool plasma loops appear connecting the two ribbons. The height of such loops can reach an altitude of 100 000 km and the distance between the ribbons increases with time after the flare maximum, first rapidly ($\sim$ 50 km s^{-1}), then more slowly ($\sim$ 1 km s^{-1}). The post-flare loops are long-lived features and may persist for more than 10 hours (Rompolt, 1993; Schmieder *et al.*, 1994). During the first phase they may appear bright on the disk in the Hα line and later they become typically dark (e.g., Gu *et al.*, 1992). Their feet are enchored in the flare ribbons. Large downflows are observed along the legs of the loops sometimes decelerated as compared to free fall motions (Heinzel, Schmieder, and Mein, 1992). The brightness of the loops is not uniform but concentrated in bubbles (Rompolt, 1993). These inhomogeneities could explain certain discrepancies between some observations and MHD models. Derived from NLTE radiative transfer diagnostics, the gas pressure of the loops ranges between about 0.1 and 5 dyn cm^{-2} and the electron density between 10^{10} and 10^{12} cm^{-3} (Švestka *et al.*, 1987; Heinzel, Schmieder, and Mein, 1992; Schmieder, 1992).

Relatively recently systems of hot loops have been found associated with cool loops, according to different observing campaigns: during an eclipse (Hanaoka, Kurokawa, and Saito, 1986), in UV (Hiei and Widing, 1979; Cheng, 1980), in X-rays (Švestka *et al.*, 1987) and in radio wavelengths (Velusamy and Kundu, 1981; Rompolt *et al.*, 1990; Trottet *et al.*, 1993, and references therein). Hanaoka, Kurokawa, and Saito (1986) observed a small helmet structure with a cusp and a streamer at the top with confined Ca IV emission. During *Skylab* mission, Cheng observed a series of loops in different lines from UV temperatures to coronal ones, overlaying each other as the temperature increases. Švestka *et al.*, using combined Hα and X-ray observations (HXIS/FCS/SMM), were the first to study the relationship between cool and hot loops for a single event (November 6, 1980). In their study the hot and cool loops appear spatially separated and extend towards higher altitudes with time. Continuous rise of large coronal structures has been confirmed to be common by *Yohkoh*/SXT (Ogawara *et al.*, 1991).

To explain the dynamics of loop systems, Sturrock (1968) and later Kopp and Pneuman (1976) proposed magnetic field lines attached to the photosphere and extending into the corona, continuously reconnecting to form magnetic loops at the base of the corona. Later on, Forbes and Malherbe (1986) studied a complete MHD reconnection model based on this configuration, explaining the replenishment of the loop by chromospheric ablation. By introducing a simple order of magnitude scaling relation for thermal conduction and radiative cooling in the model, Forbes, Malherbe, and Priest (1989) evaluated the relationship between the parameters of the hot and the cool plasmas.

In this paper we use coordinated observations made in Hα at Pic du Midi (and complemented by Wrocław images and Ondřejov spectra) together with the *Yohkoh*/SXT images to study the relationships between cool and hot loops observed after a large X-ray flare on June 25 and 26, 1992. This is the first time that high

TABLE I

List of available observation times (in UT). The instruments on Pic du Midi and in Wrocław were observing the Hα line. The MFS in Ondřejov provided several optical lines.

SXT	Ondřejov	Pic du Midi	Wrocław
06:56–07:19		07:08, 07:18	
	07:40–07:45		07:35, 07:45
08:12–08:55		08:33	08:08, 08:28
	09:08–09:36	09:36–09:38	09:30
10:27–10:31			10:12, 10:56
			11:42, 12:40

spatial resolution Hα and X-ray observations are made simultaneously. From these data we derive the plasma temperature and electron density in both hot and cool loops and these parameters, together with the co-alignment analysis, are then used to study the temporal evolution (dynamics and energetics) of the post-flare loop system.

2. Observations

A huge system of post-flare loops was developing on the west limb on June 25 and 26, 1992. The NOAA bulletin reports the occurence of an X3.9 class flare on June 25 between 19:47 and 22:29 UT with a maximum at 20:11 UT in the active region AR 7205 located at N09 W67. According to GOES an M1 class flare (at 04:10 UT) and a C3 class flare (between 06:55 UT and 07:08 UT, maximum at 07:00 UT) were registered on June 26. The loop system persisted for more than 16 hours after the X-flare and has been followed by *Yohkoh*/SXT (Anwar *et al.* 1994). The available data begin more than two hours after the X-flare maximum, during the decay phase of the flare between 22:56 UT on June 25 and 10:31 UT on June 26.

The system of loops was well observed in a coordinated, ground-based campaign, particularly at the Pic du Midi, Ondřejov, and Wrocław observatories with, respectively, the Multichannel Subtractive Double Pass Spectrograph (MSDP), the Multichannel Flare Spectrograph (MFS) and the Wrocław small coronagraph. Table I shows the corresponding observing times of the different instruments (note that SXT was also observing before 06:56 UT). We have a good sample of coordinated observations during three and half hours from 07:00 to 10:30 UT on June 26.

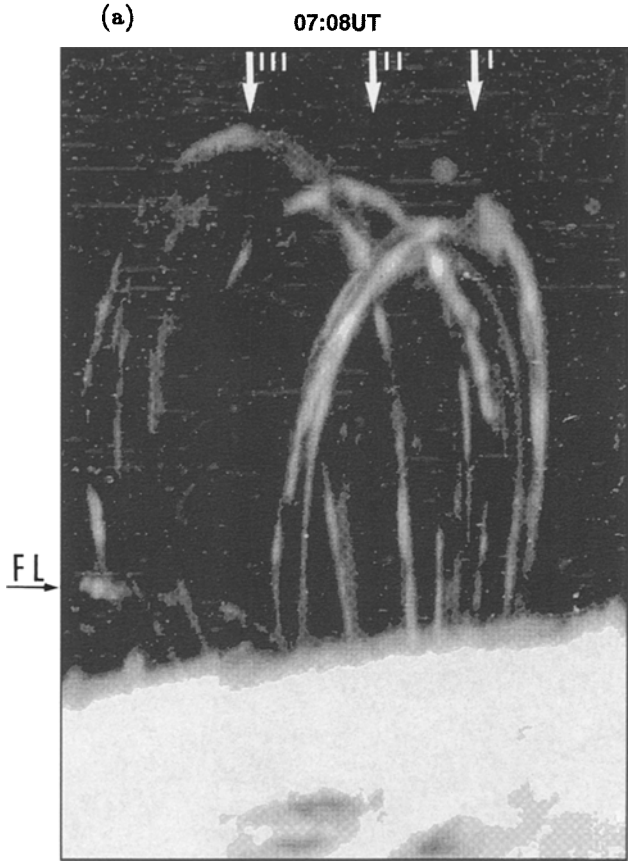

Fig. 1a.

Fig. 1a–c. Cool flare loops observed with the MSDP spectrograph at Pic du Midi in Hα (maximum intensity) for three times (a) 07:08 UT (110″ × 150″), (b) 08:33 UT (110″ × 160″) (c) 09:37 UT (110″ × 160″). Note that the limb is not the real limb of the chromosphere but the limit of the artificial moon. West is up, north is towards the left, approximatively. The loops formed an arcade which consists mainly of 3 systems (I, II, III).

2.1. INSTRUMENTS

2.1.1. *SXT Instrument*

The Soft X-ray Telescope (SXT) on board *Yohkoh* satellite has taken X-ray images using thin Al 0.1μm and thick Al 12μm filters (Tsuneta *et al.* 1991). The data were obtained in the *full* resolution mode (pixel unit = 2.46 arc sec), with 64 × 64 and 128 × 128 pixel field of view in FLARE mode and in QUIET mode, respectively.

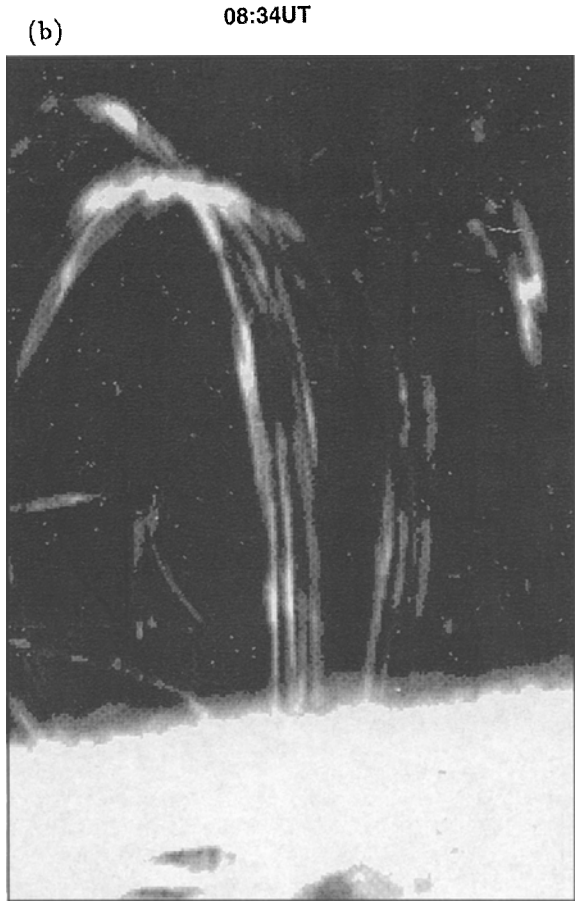

Fig. 1b.

2.1.2. *MSDP instrument*

The Multichannel Subtractive Double Pass Spectrograph (MSDP) used for these coordinated observations was operating at the Tourelle telescope on Pic du Midi. The MSDP observations of AR 7205 are listed in Table I. Three sets of observations are available, each lasting a few minutes. The MSDP provides 11 different wavelength channels of the same 2-D area, an elementary field of view, of the Sun (Mein, 1991). Photographic densities are transformed into relative intensities using calibration curves deduced from reference profiles obtained by averaging the observed profiles in quiet-Sun areas on the disk. The observations were obtained in the Hα line with a wavelength separation of 0.30 Å between channels. These data allow us to reconstruct, by interpolation, a line profile for each pixel in the field of view. The standard processing method uses the wavelength shift between the centers of two $\Delta\lambda$ chords (0.6 Å and 0.9 Å) in the active profiles and in the reference profiles to determine the Doppler shift, and the relative depths of the chords to determine the relative intensities, ΔI, for each pixel. Maximum-intensity maps of

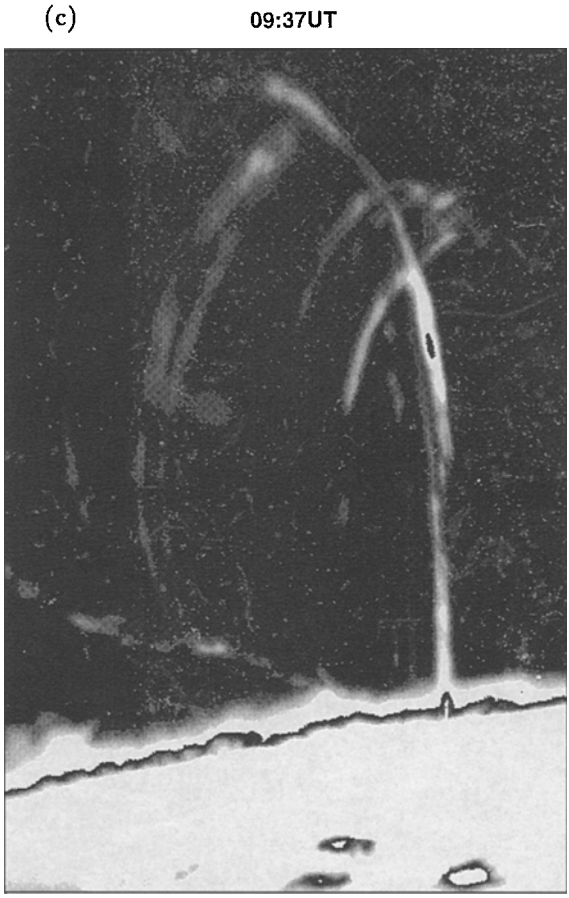

Fig. 1c.

a composite image, obtained by adding 4 to 5 elementary fields of view (124 × 900 pixels) for three different observing times, are displayed in Figures 1(a–c). The spatial resolution of the images is of the order of 0.5 arc sec. The pixel unit is 0.25 arc sec. Maps of intensity and Doppler shifts corresponding to $\Delta\lambda = 0.6$ Å are displayed in Figures 2(a) and 2(b). The spectral range is limited to 2.4 Å, therefore mass motions with Doppler shifts higher than 35 to 40 km s^{-1} cannot be detected, even in the extreme channels. In Figures 2(a) and 2(b) parts of the loops where the intensity is too low or the Doppler shifts too high cannot be seen.

2.1.3. *MFS*

The spectra of the hydrogen, helium, and Ca II lines obtained with the Multichannel Flare Spectrograph (MFS) in Ondřejov have been taken simultaneously with exposures ranging from 5 to 9 s and the dispersion 1 Å,mm^{-1}. The CCD Hα slit-jaw video camera was in operation during the observations, which allows one to fix the

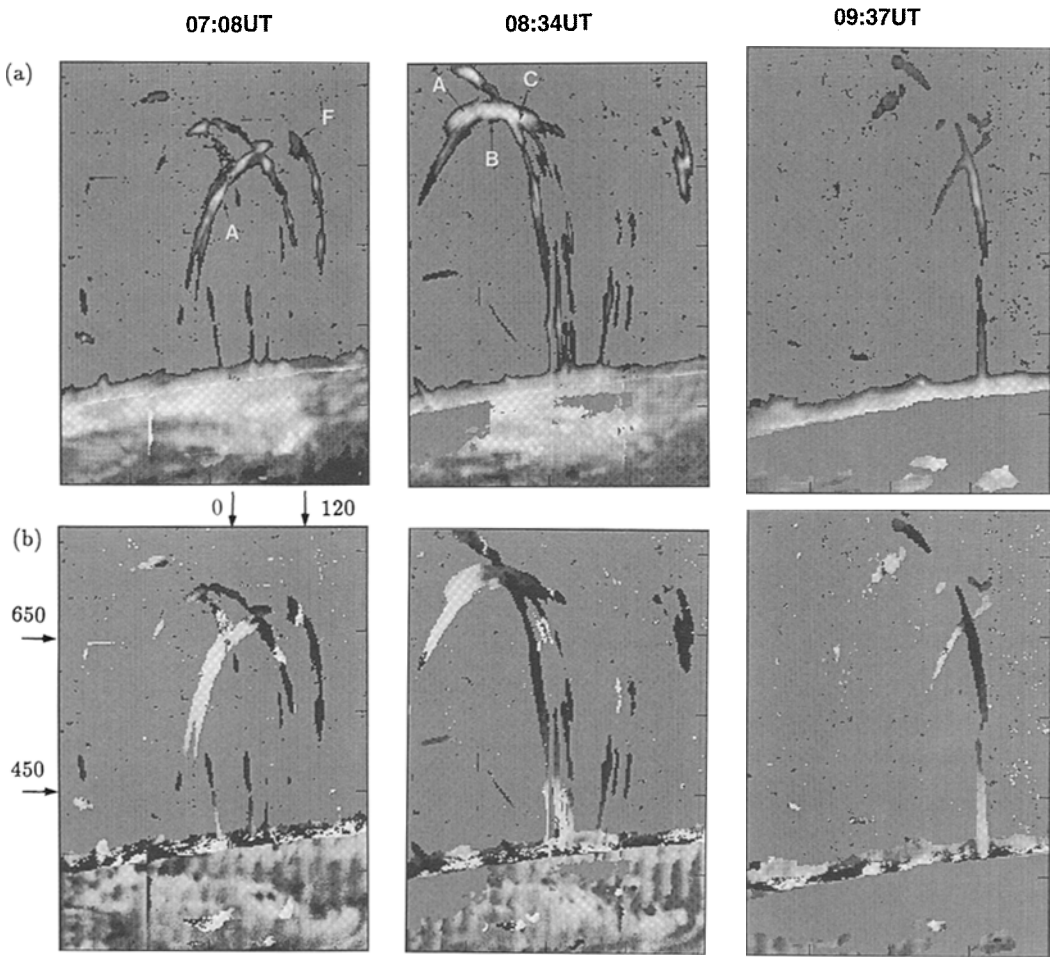

Fig. 2. Cool flare loops in H$\alpha\pm$0.3 Å observed with the MSDP: (a) intensity fluctuations (bright is white), (b) Doppler shifts (white/black corresponds to blueshift/redshift). The letters indicate the points from which we presented the profiles in Figure 7. When the intensity is too low, the intensity fluctuations and the velocity in the Hα wings at 0.3 Å cannot be computed. These points appear grey, as the sky does. The unit of the axis is around 20 000 km. North is towards the left.

position of the slit within the loop structures and provides us with the Hα images which can be compared to the MSDP ones (Heinzel *et al.*, 1994).

2.1.4. *Small Coronagraph*

The small coronagraph of the Wrocław observatory was tracking the post-flare loops. Several frames were obtained with exposures of $\frac{1}{4}$ to $\frac{1}{8}$ s. They demonstrate the development of the loops during three hours.

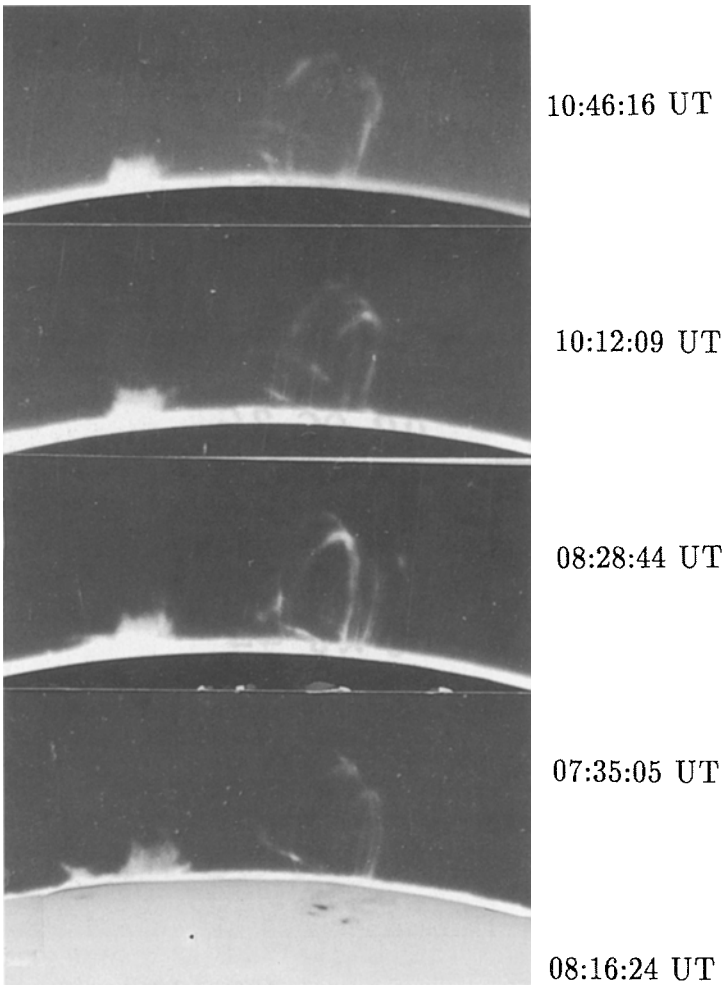

Fig. 3. Cool loops observed with the small coronagraph in Wrocław in Hα (courtesy of B. Rompolt and P. Rudawy). At 08:16:24 UT we see a composite Hα and white-light images. West is up.

2.2. EVOLUTION OF THE COOL LOOPS

In Figure 3 we have selected some of the observations made with the small coronagraph in Wrocław. We present images where the loops look different. A white-light image shows AR 7205 on the disk.

At 07:35 UT we notice a low and dense prominence to the north of the loop system which is less visible at the end of the sequence (12:00 UT). The system of loops consists of two different kinds of structures; some loops are relatively vertical while one of them (a flaring loop, see the discussion in the next sections) has an inclination of 30° with respect to the limb. These two systems of loops

have different natures. We will focus on the vertical loop systems. Between 07:35 and 10:40 UT we can distinguish three different subsystems or arcades of loops. At 07:35 UT a low system, I, with an altitude of $\sim$ 50 000 km is well visible. This system reaches an altitude of 64 000 km at 08:08 UT and is fading at 08:28 UT. A second system, II, also visible at 07:35 UT with an altitude of 68 000 km, has considerable brightness at the top, lasting from 08:28 UT to 10:12 UT. The highest system, III, appears at 08:28 UT and is still well visible at 10:12 UT with an altitude of 88 000 km. Later on at 10:46 UT only the legs of this system are visible, and they look like open structures. At 10:56 UT some material seems to be no longer attached to the loops. At 11:55 UT only footpoints are visible, but at 12:40 UT small low loops appear.

From the evolution of each system of loops we can derive approximately an ascending velocity of the loop system $v_l \simeq 1.4\,\mathrm{km\,s^{-1}}$. The footpoints of the loops are tied in the active region along a line inclined by an angle of $\sim 40°$ with the meridian, located on the disk more than 10 000 km east of the limb (in projection). If we take into account this distance, the average altitudes of loops projected into the the plane of the sky, and assuming the perpendicular orientation to the solar surface at the beginning of their appearance on Wrocław pictures, are:

system I:	$\sim$ 65 000 km	at 07:35 UT
system II:	$\sim$ 80 000 km	at 07:35 UT
system III:	$\sim$ 95 000 km	at 08:32 UT

We already noticed that the evolution of individual loops is difficult to follow. Different magnetic field lines seem to be filled by plasma, higher ones as time goes on.

2.3. Co-alignment with X-ray observations

For the two first sets of MSDP observations, SXT images are available, and a co-alignment has been made by using the SXT software package. First white-light and SXT images have been superimposed, both of them obtained during the same time series, then these composite images have been coaligned with Hα images by using the sunspots and the flaring loop (noted FL in Figure 1) as a reference (which is relatively stable in the time interval from 07:00 to 08:33 UT). The Hα loops are located just below the hot loops; their tops are almost tangential (Figure 4). With respect to the spatial resolution of the SXT images (2.46 arc sec) we estimate the height difference between hot and cool loop systems $\Delta h_l \simeq 3$–4 arc sec, distance which is equivalent to the diameter of Hα loops at the top (see Section 3.1). With a velocity of the loop system of $v_l \simeq 1.4$ km s^{-1}, this leads to a growing time $\Delta t_l = \Delta h_l / v_l \simeq 1500$–2000 s (see Figure5). A hot triangle visible in X-rays is located above the top of the loops, suggesting that there is a reconnection point as predicted by the model of Forbes and Malherbe (1986). The legs are weaker than the top of the loops and they are inhomogeneous. Just before the C3 flare a very

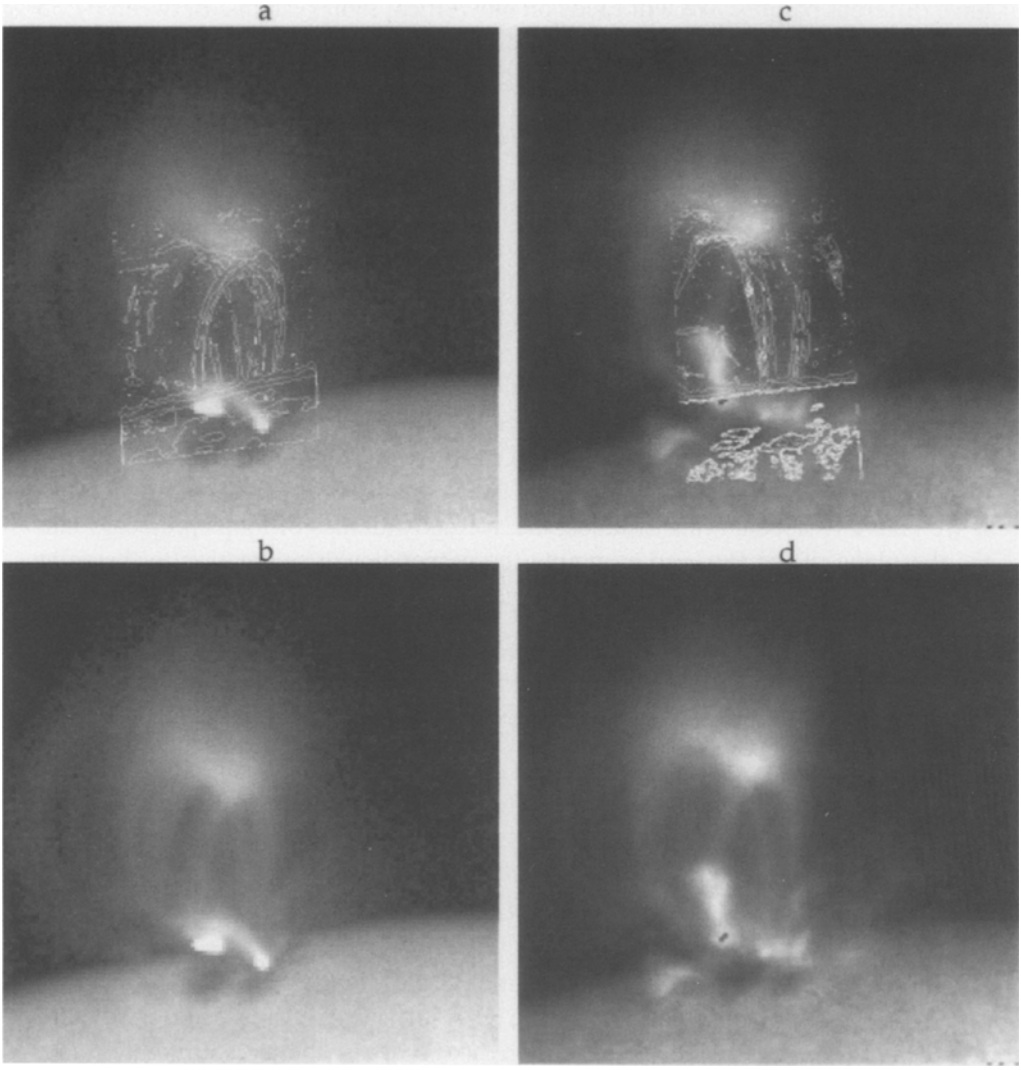

Fig. 4. Post-flare loops observed with *Yohkoh*/SXT in X-rays: (a) with Al 0.1 filter, composite image with white light (Na band), (b) with superimposed contours in Hα at 07:08 UT, (c) Al 12 filter, composite image with white light (Na band), (d) with superimposed contours in Hα at 08:33 UT. Note that the limb is not the real limb of the chromosphere but the limit of the artificial moon.

bright low loop appears on the disk (this may also be an enhancement of brightness on the disk of the ribbons). During the flare, SXT was working in FLARE mode and focusing on the brightest point, which was at the top of the loop. In Hα we do not see any significant change in the loop, only some enhancement of brightness on the disk which can correspond to a brightening of the remnant ribbons. Around 08:33 UT the leg is particularly bright near its foot in X-rays but we do not see any corresponding Hα loop because the material is too hot.

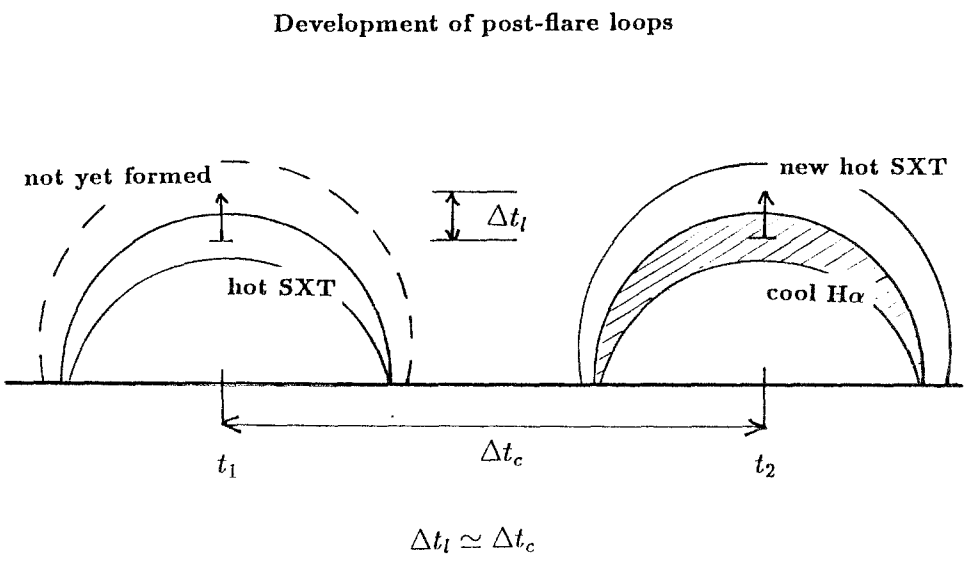

Fig. 5. Development of the post-flare loop system. Δt_l and Δt_c are respectively the characteristic growing time and the cooling time of the loops

The X-ray loops seem to be stable and their global ascending velocity, as measured between 04:50 UT and 08:55 UT, is of the same value as that obtained for cool loops.

3. Velocity Field and Integrated Intensity in Hα

3.1. BRIGHTNESS INHOMOGENEITY

The inhomogeneity of the loops appears clearly in the MSDP images (Figures 1 and 2). The loops are visible when they are filled with material. At 08:33 UT tops of the loops are brighter than the legs. This may be due to the 'agglutination' of several loops. We have followed some bubbles along one leg of a loop (Figure 6) and deduced a mean descending velocity in the plane of the sky, v, around 70 km s^{-1} for the middle part of the leg. The velocity increases substantially from top to bottom. The loop legs seem thinner near the limb than near the top. The apparent geometrical thickness of the loops around the top was estimated from the halfwidths of Hα intensity profiles as measured across the loop. It amounts to about 2000 km, but the real thickness can be somewhat smaller due to the superposition of several loops along the line of sight. In our derivation of electron densities we need to know the real thickness of the loop. As a typical value we thus take $D = 2000$ km. Even if more than one loop is occasionally seen (but unresolved) along the line of sight, the enhanced D (i.e., geometrical thickness) will be compensated by the effect of the filling factor and thus $D = 2000$ km seems to be a reasonable estimate.

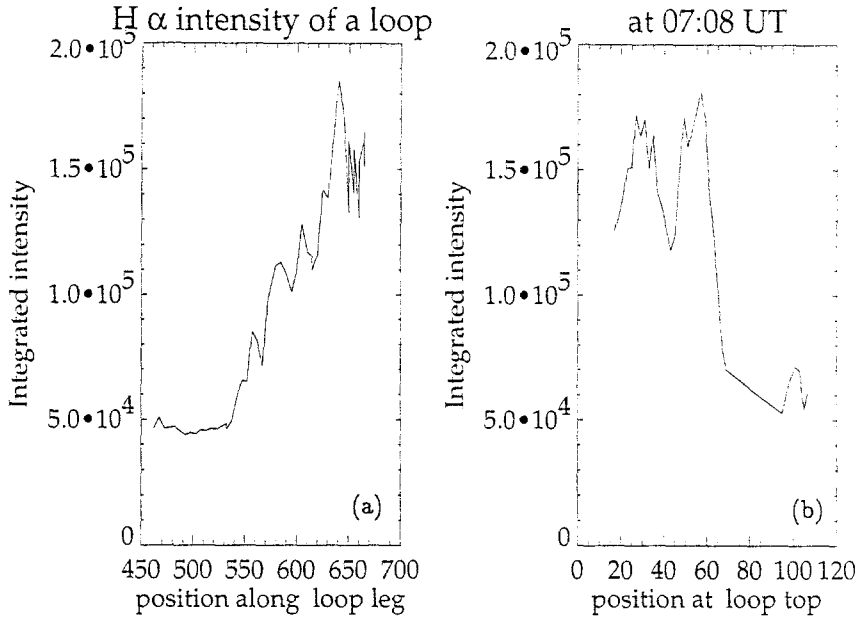

Fig. 6. Integrated Hα intensities (erg s^{-1} cm^{-2} sr^{-1}) along a leg of the post-flare loop (a) along a leg, (b) at loop top at 07:08 UT. The numbers along the x-axis represent the pixels which are indicated in Figure 2(b), in the vertical direction for (a) and in the horizontal direction for (b). The pixel size is 0.25 arc sec.

We do not see any shrinking of the loops as suggested by Švestka *et al.* (1987) for another event. However, contrary to their observations we follow our event during its late gradual decay phase.

3.2. DOPPLER SHIFTS

Due to the perspective effect the right, or south, legs of the loops are blue shifted near their footpoints and red shifted elsewhere. The Doppler shifts of the northern legs have a reversed behaviour. We conclude that the material is falling down from the top to the footpoints of the loops as is commonly observed (Schmieder, 1992).

In the legs the profiles are narrow (Figure 7 (a) profiles ABC). The Doppler velocity v_D reaches the maximum detectable value 40 km s^{-1} . At the top the profiles are broader or double-peaked because of the integration of several loops along the line of sight (Figure 7: (b) profiles ED and (c) profiles AB). To obtain the true velocity, we have to reconstruct the true shape of the loops (see, e.g., Loughhead, Wang, and Blows, 1983; Xu Ao, 1987; Heinzel, Schmieder, and Mein, 1992).

We deduce a mean value of the flow velocity in the middle part of the legs:

$$V = \sqrt{v_D^2 + v^2}\,.$$

Following the bubbles, we have deduced a mean value of v (velocity in the plane of the sky) of about 70 km s^{-1} . A value of 80 km s^{-1} seems to be reasonable for V.

3.3. Hα LINE PROFILES AND INTEGRATED INTENSITY

During the data processing, the MSDP Hα profiles of the loops have been automatically normalized to the observed local continuum, $I(\lambda)/I^{\rm obs}_{c,\rm loc}$. This local (i.e., observed close to the limb, $\sin\theta = 0.9$) continuum was detected with a density attenuator which reduces the intensity by a factor of 0.13. Therefore, $I^{\rm obs}_{c,\rm loc} = 0.13 \times I_{c,\rm loc}$. Moreover, due to the limb darkening, we obtain $I_{c,\rm loc} \simeq 0.7 \times I_c$, where I_c is the disk-center continuum intensity close to Hα. In order to transform the observed ratio $I(\lambda)/I^{\rm obs}_{c,\rm loc}$ to $I(\lambda)/I_c$ (i.e., the normalization to the disk-center continuum intensity), we use the following relation, already used by Wiik, Heinzel, and Schmieder (1992):

$$I(\lambda)/I_c = 0.13 \times 0.70 \times [I(\lambda)/I^{\rm obs}_{c,\rm loc}] \, .$$

Multiplying by 10^2 we get finally the loop intensity in % of I_c – see Figure 7 (full profiles). In Figure 7 we also display the reference profiles obtained by averaging the observed disk profiles (dashed profiles). These reference profiles have been multiplied by a factor $(0.13)^{-1}$ in order to get the same units (i.e., % of I_c) as for (full) loop profiles.

Using the loop emission profiles (Figure 7), we have evaluated the Hα-line integrated intensity

$$E = \int I(\lambda)\, {\rm d}\lambda = I_c \times \int I(\lambda)/I_c \, {\rm d}\lambda \; [\text{Å}] \, .$$

E is given, as an example, in Figure 6 and in Table II (in c.g.s. units, erg cm^{-2} s^{-1} sr^{-1}), $I_c = 2.836 \times 10^6$ erg cm^{-2} s^{-1} sr^{-1} $Å^{-1}$.

The density attenuator was replaced before each set of observations (which lasted a few minutes around the times given in Table I) by an artificial moon. The limb which is drawn on the Figures 1 and 2 is not the real limb of the chromosphere but the limit of the scattered light due to the artificial moon. This explains the arbitrary position of the limb compared to the X-ray limb.

A mean value of the integrated intensity at the top of the loops is thus around 10^5 erg s^{-1} cm^{-2} sr^{-1} (Table II). This value, derived from MSDP data, is consistent with a mean value obtained at 07:43:10 UT by MFS in Ondřejov (see the Hα profiles presented in Heinzel *et al.*, 1994). However, in the loop legs, MSDP gives higher intensities as compared to MFS spectra. We ascribe this difference to a lower spatial resolution of the MFS (caused by unfavourable seeing conditions) and to the fact that at different times different bubbles appear along the loop legs. This point will be discussed in another paper devoted to analysis of MFS spectra.

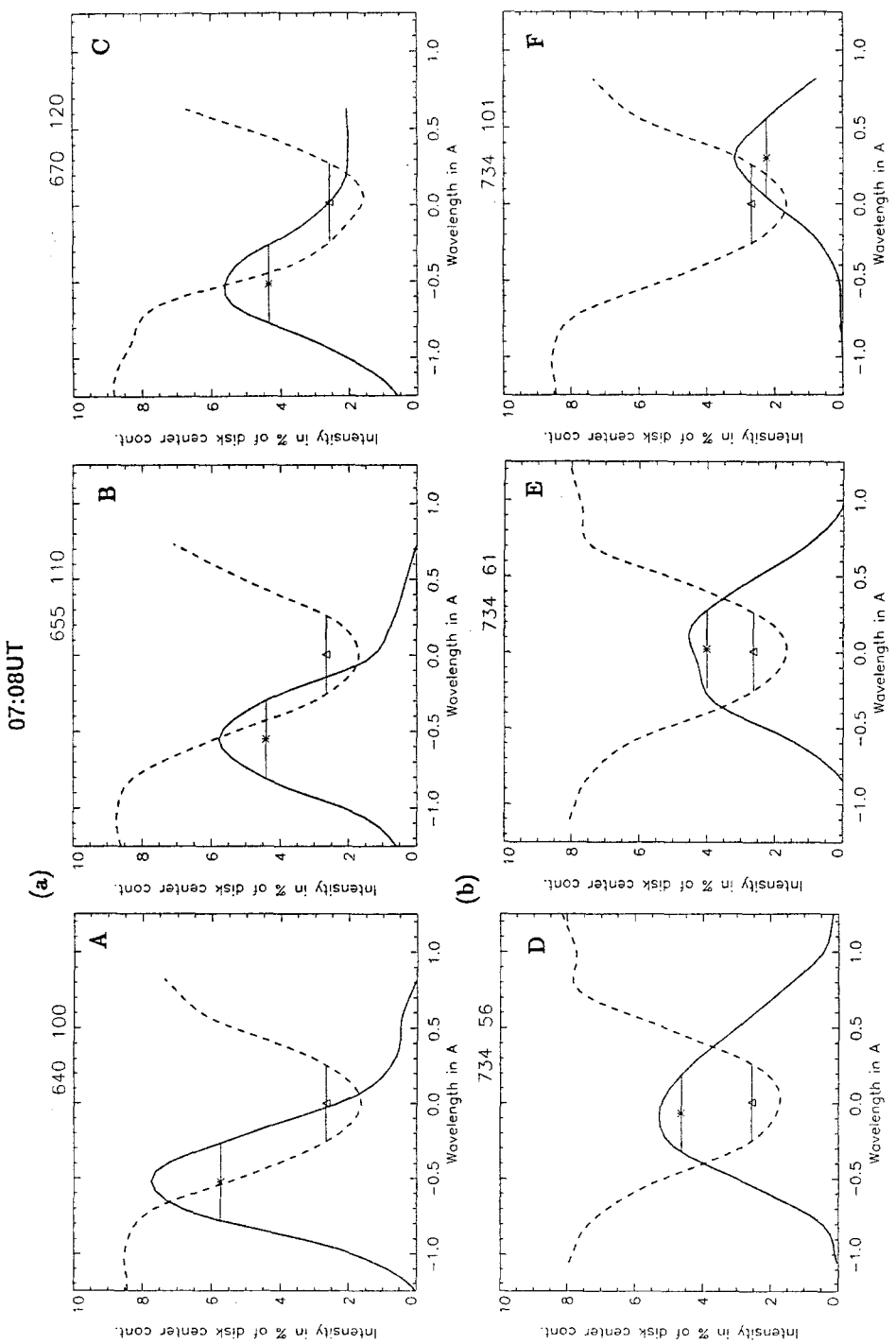
07:08UT
(a)
(b)
A
640 100
B
655 110
C
670 120
D
734 56
E
734 61
F
734 101
Intensity in % of disk center cont.
Wavelength in A
-1.0
-0.5
0.0
0.5
1.0
0
2
4
6
8
10

Fig. 7a–b.

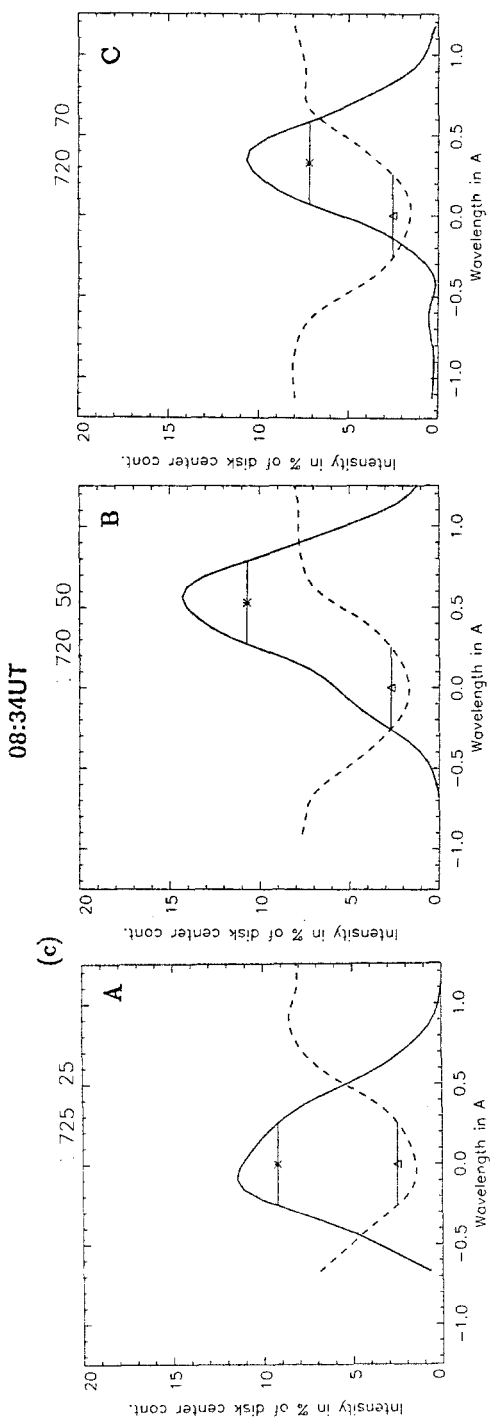

Fig. 7c.

Fig. 7. MSDP Hα profiles (a) along a leg and (b) near the loop top at 07:08 UT, A–F correspond to Table II, and (c) at the top at 08:33 UT. The points A–F and A–C and their coordinates, which are written in each panel, are also indicated in Figure 2. The dashed profiles are the reference profiles obtained by averaging the profiles observed on the disk close to the limb. They must be multiplied by a factor $(0.13)^{-1}$ to get the intensity in % of I_c.

TABLE II

Integrated intensity of the Hα line at the top and in one leg of the loop at 07:08 UT (v_D negative/positive corresponds to redshift/blueshift)

Point	Altitude from the top in km	$i-j$ coordinates	v_D km s^{-1}	Integrated intensity 10^5 c.g.s. units
A	17 000	640–100	+31	1.9
B	15 000	655–110	+33	1.5
C	10 000	670–120	+31	1.8
D	0	734–56	+4	1.8
E	0	734–61	+0.3	1.4
F	0	734–101	−18	0.7

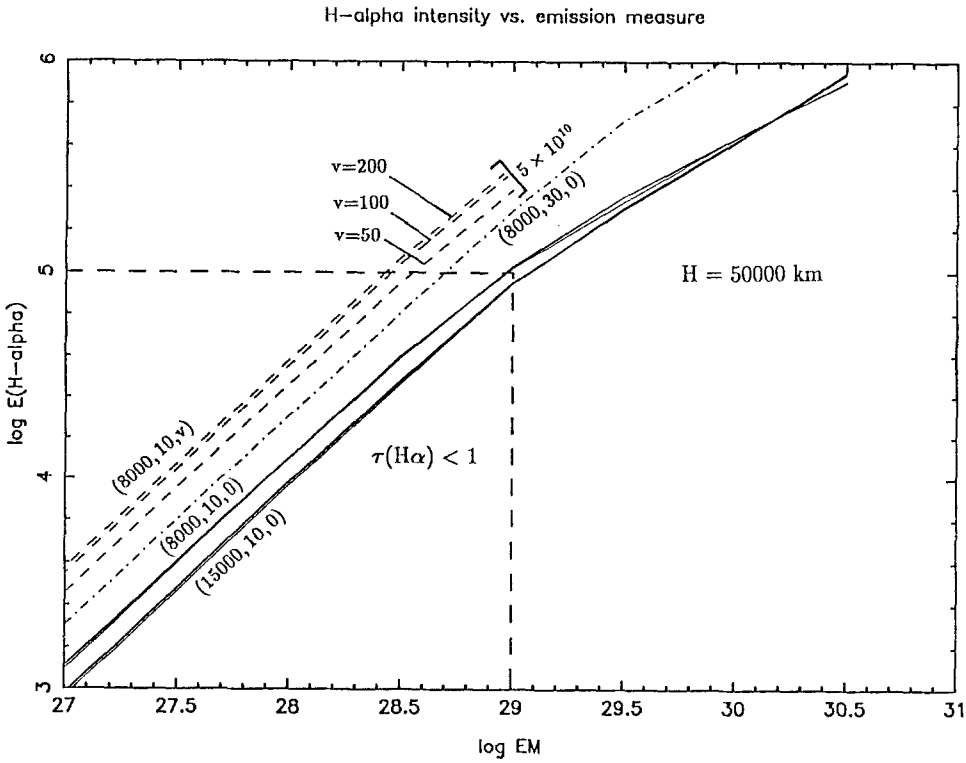

Fig. 8. Log $E(\mathrm{H}\alpha)$ versus log (EM) . The parameters in parentheses are, respectively, the temperature, the microturbulent velocity, v_t, and the vertical component of the flow velocity. For $v \neq 0$ only one value of the electron density is considered (5×10^{10} cm^{-3}). Double splitting of the full lines is due to the two different heights considered (50 000 and 100 000 km). Inside the dashed box $\tau(\mathrm{H}\alpha) < 1$.

4. Spectral Diagnostics of Cool Loops

4.1. EMISSION MEASURE AND ELECTRON DENSITIES OF COOL LOOPS

Assuming an averaged value of electron density n_e, the emission measure is $EM = n_e^2 \times D$ with D being the geometrical thickness along the line of sight. Theoretical correlation between EM and the integrated Hα intensity $E(\mathrm{H}\alpha)$ was revealed recently by Gouttebroze, Heinzel, and Vial (1993) and further discussed by Heinzel, Gouttebroze, and Vial (1994). These authors found an almost *unique* relation between E(Hα) and EM, depending only weakly on the kinetic temperature. This theoretical correlation was constructed on basis of 140 NLTE models of prominence-like structures (for details see Gouttebroze, Heinzel, and Vial, 1993), computed for various temperatures, gas pressures and geometrical thicknesses. For all models, these authors used the microturbulent velocity $v_t = 5\,\mathrm{km\ s^{-1}}$ and the prominence height was 10 000 km. In Figure 8 we plot this kind of correlation recomputed by a fast NLTE code (see Wiik, Heinzel, and Schmieder, 1992) for a realistic range of Hα loop temperatures (8000–15 000 K), for $v_t = 10\,\mathrm{km\ s^{-1}}$ and two heights $H = 50\,000$ km and $H = 100\,000$ km, corresponding to our MSDP observations. We see that the correlation is not very sensitive to temperature and almost insensitive to height variations (this behaviour is explained in Heinzel, Gouttebroze, and Vial, 1994). In this paper we use this correlation to estimate the electron density in cool loops. In fact the estimate by this new method is not affected so much by the uncertainty in D (i.e., the filling factor), since EM depends on n_e^2 – for discussion of this point see also Heinzel, Gouttebroze, and Vial (1994). Note also that some other processes which can give rise to additional hydrogen ionization, like strong soft X-ray irradiation by hot loops (Heinzel *et al.*, 1994), will not affect this correlation curve since it gives the relation between E(Hα) and the *given* electron density.

To derive n_e at the top of the cool loops, we start from E(Hα) given in Table II. The mean value over the MSDP pixel size, 0.25 arc sec, is around $E = 1 \times 10^5$ erg cm^{-2} s^{-1} sr^{-1}. The examination of individual Hα profiles gives an estimate of the Doppler width about 0.4 Å (Figure 7), which corresponds to temperatures around 10^4 K and $v_t \simeq 10 - 15\,\mathrm{km\ s^{-1}}$. With these data (from Figure 8) we get $EM \simeq 10^{29}\,\mathrm{cm^{-5}}$. In this case we are just on the border of the optically-thin region (see Figure 8). In Section 3.1 we estimated the loop-top thickness $D \simeq 2000$ km, taking into account projection effects. The corresponding electron density is $n_e \simeq 2.2 \times 10^{10}\,\mathrm{cm^{-3}}$. If we would change our D by a factor of four, for example, then n_e will be changed by no more than a factor of only two, which is still a rather good estimate. We will use this electron density in the subsequent analysis of the energy balance.

4.2. EMISSION MEASURE EXCESS IN LOOP LEGS

The integrated intensity of Hα in the upper parts of the loop legs is higher compared to the integrated intensity at the top. This looks rather surprising because we do not expect any density or temperature increase for downflowing plasma. Also the diameter of the loop is almost the same for the top and upper legs. Taking as an example data from Table II for position A (see also Figure 1), we get $E = 1.9 \times 10^5$ c.g.s., which gives – using the same procedure as for the top of the loops – $EM \simeq 2.7 \times 10^{29}$ c.g.s., i.e., more than half an order higher than EM at the top of the loops. We explain this emission-measure excess by the Doppler brightening effect (DBE) in the Hα line (Hyder and Lites, 1970; Heinzel and Rompolt, 1987).

As already mentioned, our MSDP observations indicate large downflow velocities in the loop legs. For point A (see Table II) the vertical component of the flow velocity reaches about 50 km s^{-1} and thus for $n_e < 5 \times 10^{10}$ cm^{-3} the increase of E(Hα) due to DBE should be approximately a factor of two relatively to the static loop (Heinzel and Rompolt, 1987, see their Figures 7 and 10 for various temperatures). Using Figure 7 of Heinzel and Rompolt (1987), we include the additional curves into our Figure 8, indicating the correlation between E(Hα) and EM when the flow velocities (and thus DBE) are taken into account. Note that a similar brightening can arise in the case of very large turbulent velocities, as also demonstrated in our Figure 8 (using Figure 11 from Heinzel and Rompolt, 1987). Now using the curve labeled 50 km s^{-1}, the E(Hα) for the loop leg leads to comparable or even somewhat lower EM, which is quite acceptable.

5. Emission Measure and Temperature of Hot Loops

The SXT images display the post-flare loops versus time (Figures 4 and 9). Temperatures and emission measures of the flare loops have been derived by using the filter-ratio method defined by Vaiana *et al.* (1977) and developed by Tsuneta *et al.* (1991), Hara *et al.* (1992), and Anwar *et al.* (1994). The temperature at the loop top shows a decay temporal behaviour and its value is around 5.5×10^6 K at the time of interest (07:00–10:00 UT) the *log* of averaged emission measure is decreasing from 46.7 at 22:30 UT to 44.6 ten hours later. Anwar *et al.* (1994) derive an emission measure of $10^{44.6}$ cm^{-3} in an area of 30×53 pixels, i.e., $\sim 4.5 \times 10^{19}$ cm^2 between 07–08 UT.

With an effective area reduced to 2×2 pixels (1.2×10^{17} cm^2) we could expect an emission measure of 1.7×10^{45} cm^{-3} by extrapolation of measurements made between 3:40 and 5:00 UT. Then

$$EM = 1.7 \times 10^{45} / 1.2 \times 10^{17} \simeq 10^{28} \text{ cm}^{-5} .$$

Since this value of EM is now in standard units, we can compare it directly with that derived for cool loops (tops) and this will give us the *relative ratio of the*

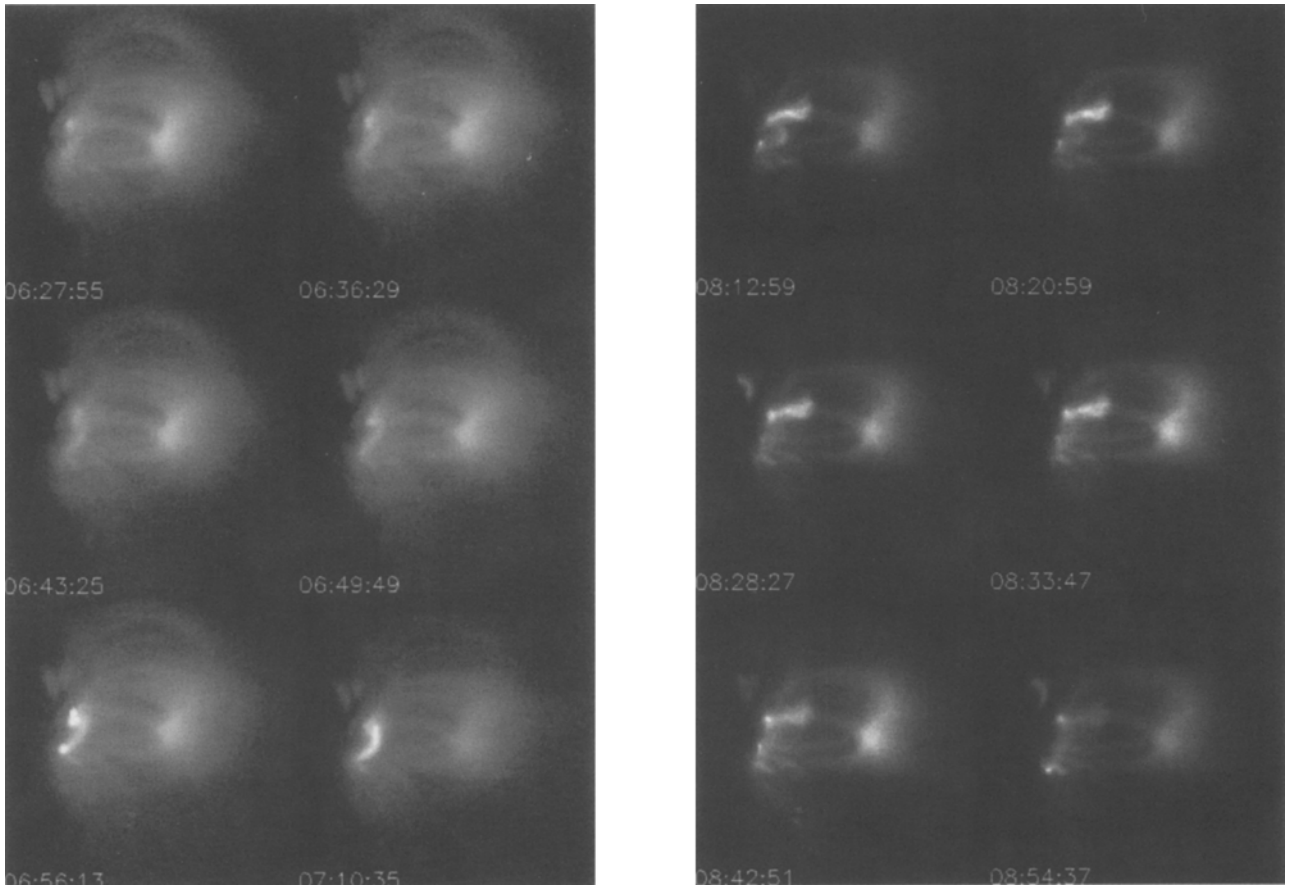

Fig. 9. Some soft X-ray images showing the evolution of the hot loops during two orbits. (a) from 06:27:55 to 07:10:35 UT with Al 0.1 filter and with no calibration used in the data processing , (b) from 08:12:59 UT to 08:54:37 UT with Al 12 filter and with calibration.

electron densities in hot and cool loops (denoted as α), which is an important plasma parameter for post-flare loops (Forbes, Malherbe, and Priest, 1989). Therefore,

$$\alpha = \frac{n_e^h}{n_e^c} \simeq \left(\frac{EM_h}{EM_c}\right)^{1/2} \simeq 0.32. \quad (1)$$

In this ratio, we assumed that the geometrical extension of hot and cool loops, at approximately the same height (position) is similar. In fact the cool loops are supposed to be the result of cooling the initially hot loops, and even in case of certain shrinking (Švestka *et al.*, 1987), the loop diameter is not altered too much.

Therefore, the electron density at the top of hot X-ray loops is about a factor of three lower than the electron density in cool loops, i.e., $n_e^h \simeq 7 \times 10^9\,\mathrm{cm}^{-3}$. Higher density in cool loops may be the result of the evaporation process which takes place during the conductive cooling phase. Indeed, we still observe in Hα weak ribbons in the chromosphere.

6. Energy Balance and Cooling Processes

In the previous sections we have analyzed the spatial co-alignment of hot and cool loops and estimated the respective electron densities and kinetic temperatures. In this section we take advantage of these unique high-resolution simultaneous data and we try to understand the global evolutionary trends in post-flare loop systems.

The whole loop system is gradually growing with an ascending velocity of about $v_l \simeq 1.4\,\mathrm{km\ s}^{-1}$ (see Section 2). From our co-alignment analysis we can derive a mean height difference between the hot and cool loops, Δh_l. Now assuming that there is no shrinking of cooler loops (see Švestka *et al.*, 1987), the time difference $\Delta t_l \simeq \Delta h_l / v_l$ should be comparable to Δt_c, i.e., to a mean cooling time which is necessary for hot X-ray loops to reach a cool Hα state observed with a time delay Δt_l. So as a working hypothesis we assume that $\Delta t_c \simeq \Delta t_l$ (Figure 5). Now we shall check the validity of this relation by evaluating the cooling time, Δt_c, and comparing it to Δt_l as directly obtained from co-alignment. This is in principle possible since we know approximately the electron densities and temperatures in hot and cool loops.

6.1. Cooling Times – Method of Evaluation

In order to estimate the time which initially hot X-ray loops need to reach the state of cool Hα plasma, we proceed here in a similar way as Švestka (1987). We assume a static loop, heated by a reconnection process to a flare temperature T_h (see Forbes, Malherbe, and Priest, 1989) and then gradually cooled to $T_c \simeq 10^4$ K. Two cooling mechanisms are considered, i.e., conductive and radiative losses. The

temporal variation of kinetic temperature T in such a loop is then schematically governed by the differential equation (Švestka, 1987)

$$\mathrm{d}T/\mathrm{d}t = -[\epsilon(T)n_e^2 + 1.1 \times 10^{-6}T^{7/2}/L^2]/3kn_e. \quad (2)$$

In this equation n_e is the electron density, L is the semi-length of the loop and k the Boltzmann constant. The plasma is assumed to be fully ionized, which is approximately valid down to temperatures around 2×10^4 K. The radiative cooling function $\epsilon(T)$, which depends only on the temperature, can be approximated in different ways. For $3 \times 10^5 < T < 3 \times 10^7$ K we use the same expression as Švestka (1987) (as given by Raymond, Cox, and Smith, 1976), i.e.,

$$\epsilon(T) \simeq 1.2 \times 10^{-19}/T^{1/2}. \quad (3)$$

Then we extend the original Švestka solutions to temperatures lower than 3×10^5 K, down to $T \simeq 2 \times 10^4$ K. To do this we use the cooling function estimate as suggested by McClymont and Canfield (1983) and used by Klimchuk and Mariska (1988) for modelling of cool solar loops

$$\epsilon(T) \simeq 3.8 \times 10^{-37}T^3, \quad (4)$$

where we have renormalized the original constant in order to get a smooth solution at $T = 3 \times 10^5$ K. For temperatures lower than 2×10^4 K, the situation becomes much more complicated due to partial ionization of the plasma, NLTE opacity effects, conduction across the magnetic field lines, etc.

The differential equation (2) was solved numerically by the fourth-order Runge–Kutta method. For constant electron densities, the method was tested against the results of Švestka (1987) – see his Figure 1. For T lower than 10^5 K, the cooling slows down and the resulting cooling time is somewhat longer as compared to Švestka. Moreover, Švestka (1987) already mentioned the possible effect of increasing electron density on the total cooling time. This increase of density may be due to evaporation processes taking place when the conductive cooling front propagates into the cool plasma – in our data we also observe higher densities in cool loops as compared to SXT loops and we see the bright Hα ribbons, an indication of the chromospheric heating and evaporation (an additional heating can be due to soft X-ray irradiation of the chromosphere, see recent models of Hawley and Fisher, 1993). Therefore, as a next step, we assumed rather schematic temporal variation of n_e, for example a linear increase from SXT values to those derived from MSDP data. In this case we obtain some intermediate cooling curves as already expected by Švestka in his paper. Note that Švestka's results were compared by Gan and Fang (1990) with their fully-hydrodynamical simulations. They found very good agreement between both approaches for cooling times longer than about 1000 s (see their Table III).

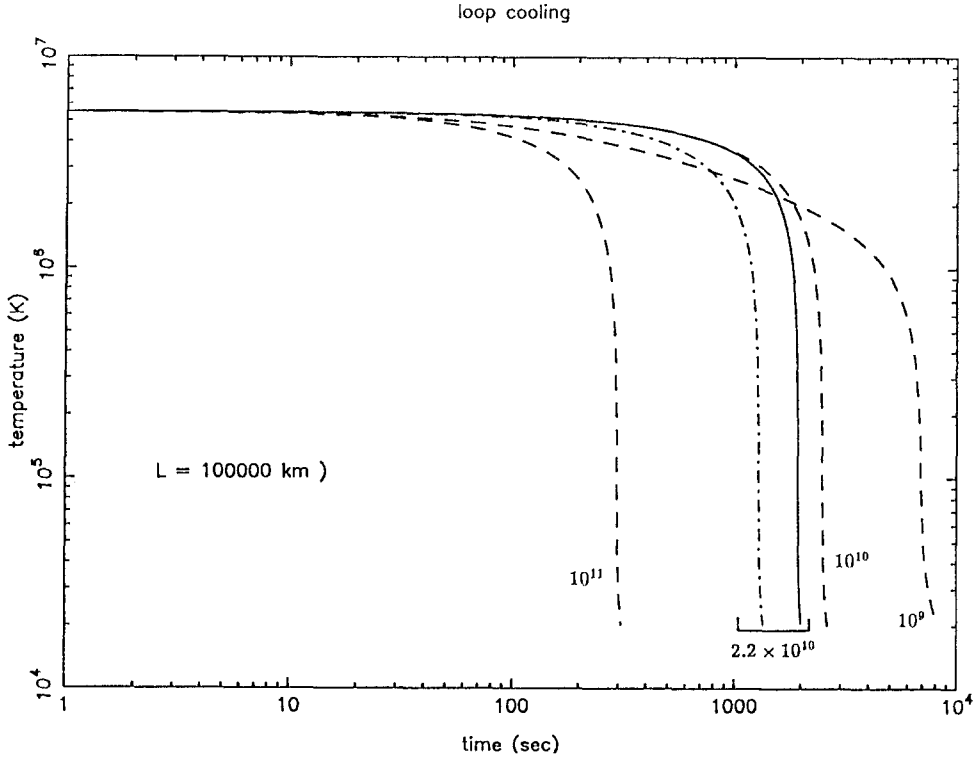

Fig. 10. Cooling of the loop with a semilength L=100000 km, for various electron densities and the initial temperature $T = 5.5 \times 10^6$ K

6.2. COOLING TIMES – RESULTS FROM SXT AND MSDP

Using electron densities and temperatures derived in the previous Section 5, we solve the energy-balance equation (1) in order to estimate the cooling time. In Figure 10 we present the results for a typical situation often met in our data, i.e., T is decreasing from $T_h \simeq 5.5 \times 10^6$ K down to $T_c \simeq 1-2 \times 10^4$ K, while the electron density increases from $n_e^h \simeq 7 \times 10^9$ cm^{-3} to $n_e^c \simeq 2.2 \times 10^{10}$ cm^{-3}. We assume a linear increase of n_e with decreasing temperature (full line in Figure 10); other possible forms give similar results. L was estimated to be around 100 000 km for loop system I having a circular shape. If the initial value of the electron density were identical with the final one, i.e., $n_e^h = n_e^c$ (as assumed in Švestka's computations), we would arrive at a somewhat shorter cooling time – see dot-dashed curve in our Figure 10. To see the general behaviour of the cooling process, we also include into this figure the solutions for other electron densities ranging from 10^9 to 10^{11} cm^{-3}, as Švestka (1987) did for his loop models. From Figure 10 it is also possible to see when the radiation cooling process (which depends mainly on the density) starts to dominate the conductive cooling (after about 10–100 s).

From Figure 10 we deduce a typical cooling time $\Delta t_c \simeq 2000$ s, quite comparable to Δt_l obtained from co-alignment analysis. Therefore, this result suggests that the hot loops as observed by SXT gradually cool to Hα ones seen by the MSDP instrument and the assumed cooling process is consistent with the scenario of the global rise of the whole loop system (Figure 5) due to subsequent reconnection of higher magnetic field lines (Forbes, Malherbe, and Priest, 1989). In our opinion, no shrinking of cooler loops is necessary to explain consistently these observations. In fact, our electron densities pertinent to cool loops are far lower than those derived by Švestka *et al.* (1987) for very bright loops observed in emission on the disk ($n_e \simeq 10^{12}\,\mathrm{cm}^{-3}$), and thus our cooling time is long enough to match well the typical growth-time of the loop system.

Concerning the accuracy of our determination of Δt_c, there are two aspects to be considered: (i) the approximate validity of the formula (2) (we already discussed this point above), and (ii) the accuracy of determination of temperatures and electron densities (or emission measures). $T_h \simeq 5 \times 10^6$ K seems to be determined rather well since we are still in the steep part of the SXT calibration curve. Increasing T_h by a factor of two – for example – leads to cooling times larger by a factor less than two. More uncertain is the emission measure EM_h. But as we see from Figure 10, even starting from $n_e^h = n_e^c$, the final cooling time is not too much shorter – see dot-dashed curve. Therefore, we can conclude that the cooling time Δt_c depends primarily on n_e^c and this is determined relatively well compared to n_e^h. Even the uncertainty in the geometrical thickness of the loops within a factor of two gives a small uncertainty in n_e^c within a factor of $\sqrt{2}$ (Heinzel, Gouttebroze, and Vial, 1994). In fact replacing $n_e^h = 7 \times 10^9 \mathrm{cm}^{-3}$ by the value pertinent to cool loops (2.2×10^{10} cm^{-3}) means that EM_h will be an order of magnitude higher which may lay within uncertainties of SXT data analysis.

7. Conclusions and Future Prospects

Cool and hot loops have been observed simultaneously in Hα with the MSDP and in X-rays with SXT/*Yohkoh* 10 hours after an X-class flare. The cool loops are found located tangentially below the hot ones, they are inhomogeneous (downward moving Hα blobs) and growing slowly upward (~ 1.4 km s^{-1}). At the top of the hot loops a triangle of hot plasma (5 to 8×10^6 K) is clearly detected, suggesting a reconnection process as proposed by Forbes and Malherbe (1986). The Hα inhomogeneities seen in Figure 2 as bubbles may be due to thermal instability during the condensation process or instability due to turbulence during the reconnection in an MHD model.

Another system of loops (flaring loops) was visible both in X-rays and in Hα. They were nearly cospatial. That is not the case for the post-flare loops.

The nearly horizontal loop had a different regime of flow, upflows along one leg and downflows along the other one. It belongs to a different kind of loop and

more or less represents a flaring loop which has a different mechanism of formation than the post-flare loops. This kind of loops is more relevant to a surge mechanism (Pikel'ner, 1969).

From detailed co-alignment analysis of Hα and SXT loop observations we have derived the growing speed of the loop system and the time delay for the visibility of cool loops. On the other hand, the cooling time was estimated using these simultaneous data, which provide the electron densities and temperatures in both hot and cool loops. The growing time was found to be quite comparable to the cooling time, which supports the scenario of post-flare loop system development as sketched in Figure 5. Moreover, under these conditions no loop-shrinking process is necessary for this particular flare. The temperature of hot SXT loops is around $T_h \simeq 5.5 \times 10^6$ K, the electron densities are 7×10^9 and 2.2×10^{10} cm^{-3} for hot and cool loops, respectively. For Hα loops this density represents a lower limit of the generally accepted values (Schmieder, 1992), which can be due to the fact that our observations correspond to a very late phase of the flare. To draw our basic conclusions, we used in this paper – for the first time – simultaneous high-resolution limb observations in soft X-rays and Hα provided by SXT/*Yohkoh* and MSDP instruments.

As a next step we plan to use the Ondřejov MFS spectra to improve the temperature and density diagnostics of cool loops. We are also working on detailed analysis of 2D MSDP Hα intensity and velocity maps, which, together with the geometrical reconstruction of the true shape of loops, will provide us with the necessary information for further studies of the cool loop hydrodynamics. Finally, in order to improve the modelling of the cooling process, we shall also consider temperatures below 20 000 K, taking into account the NLTE opacity effects.

Acknowledgements

The authors thank Drs Forbes, Malherbe and Švestka for fruitful discussions. We are very grateful to Dr Roudier for the help with Pic du Midi MSDP observations, to Drs P. and N. Mein for their assistance in the MSDP data processing and to Drs Rompolt and Rudawy for providing us with the Wrocław observations. One author (B.S.) wants to thank particularly the team of *Yohkoh* for helping her in SXT data reduction in ISAS during her stay, Dr J. Gurman for helping with the co-alignment of Hα data and X-ray images and Dr B. Bentley for the installation of the *Yohkoh* software in Meudon. P.H. acknowledges the support of the Observatoire de Meudon during the course of this work.

References

Anwar, B., Hiei, E., Hudson, H. S., Acton, L. W., Lemen, J., and Metcalf, T.: 1994, in S. Enome and T. Hirayama (eds.), *New Look at the Sun*, Kofu Meeting from September 6 to 10.

Bray, R. J., Cram, L. E., Durrant, C. J., and Loughhead, R. E.: 1991, *Plasma Loops in the Solar Corona*, Cambridge Astrophys. Ser. 18, Cambridge University Press, Cambridge.
Cheng, C. C.: 1980, *Solar Phys.* **65**,347.
Forbes, T. G. and Malherbe, J. M.: 1986, *Astrophys. J.* **302**, L67.
Forbes, T. G., Malherbe, J. M., and Priest, E. R.: 1989, *Solar Phys.* **120**, 285.
Gan, W. Q. and Fang, C.: 1990, *Astrophys. J.* **358**, 328.
Gouttebroze, P., Heinzel, P., and Vial, J. C.: 1993, *Astron. Astrophys. Suppl. Ser.* **49**, 513.
Gu, X. M., Lin Jun, Luan Ti, and Schmieder, B. : 1992 *Astron. Astrophys.* **259**, 649.
Hanaoka, Y., Kurokawa, H., and Saito, S : 1986, *Solar Phys.* **105**, 133.
Hara, H., Tsuneta, S., Lemen, J. R., Acton, L. W., and McTiernan, J. M.: 1992, *PASJ*, **44**, L135.
Hawley, S. L. and Fisher, G. H.: 1993, SSL Preprint, University of California at Berkeley.
Heinzel, P. and Rompolt, B.: 1987, *Solar Phys.* **110**, 171.
Heinzel, P., Schmieder, B., and Mein, P.: 1992, *Solar Phys.* **139**, 81.
Heinzel, P, Kotrč, P., Schmieder, B., Hiei, J., and Anwar, B. : 1994, *Space Sci. Rev.* **70**, 181.
Heinzel, P., Gouttebroze, P., and Vial, J. C.: 1994, *Astron. Astrophys.*, in press.
Hiei, E. and Widing, K. G.: 1979, *Solar Phys.* **61**, 407.
Hyder, C. L. and Lites, B. W.: 1970, *Solar Phys.* **14**, 147.
Klimchuk, J. A. and and Mariska, J. T.: 1988, *Astrophys. J.* **328**, 334.
Kopp, R. A. and Pneumann, G. W.: 1976, *Solar Phys.* **50**, 85.
Loughhead, R. E., Wang, J. L., and Blows, G.: 1983, *Astrophys. J.* **74**, 883.
McClymont A. N. and Canfield, R. C.: 1983, *Astrophys. J.* **265**, 497.
Mein, P.: 1991, *Astron. Astrophys.* **248**, 669.
Ogawara, Y., Takano, T., Kato, T., Kosugi, T., Tsuneta, S., Watanabe, T., Kondo, I., and Uchida, Y.: 1991, *Solar Phys.* **136**, 1.
Pikel'ner, S. B.: 1969, *Astron. Zh.* **46**, 328.
Raymond, J. C., Cox, D. P., and Smith, B. W.: 1976, *Astrophys. J.* **204**, 290.
Rompolt, B.: 1993, *Solar Phys.* **141**, 1.
Rompolt, B. *et al.*.: 1990, *Debrecen SPS* **7**, 206.
Schmieder, B.: 1992, *Lecture Notes in Physics* **399**, 124.
Schmieder, B., Hagyard, M. J., Guoxiang, Ai., Zhang, H. Q., Kálman, B., Györi, L., Rompolt, B., Démoulin, P., and Machado, M. E.: 1994, *Solar Phys.* **150**, 199.
Švestka, Z.: 1987, *Solar Phys.* **108**, 411.
Švestka, Z.: 1989, *Solar Phys.* **121**, 399.
Švestka, Z. and Cliver, E. W.: 1992, *Lecture Notes in Physics* **399**, 1.
Švestka, Z., Fontenla, J. M., Machado, M. E., Martin, S. F., Neidig, D. F., and Poletto, G.: 1987, *Solar Phys.* **108**, 237.
Sturrock, P.A.: 1968, *IAU Symp.* **35**, 471.
Trottet, G., Vilmer, N., Barat, C. *et al.*: 1993, *Adv. Space Res.* **13**, 9, 285.
Tsuneta, S., Acton, L. W., Bruner, M. *et al.*: 1991, *Solar Phys.* **136**, 37.
Vaiana, G. S., Van Speybroek, L., Zombeck, M. V., Krieger, A. S., Silk, J. K., and Timothy, A.: 1977, *Space Sci. Instr.* **3**, 19.
Velusamy, T. and Kundu, M. R.: 1981, *Astrophys. J.* **240**, 1130.
Xu Ao, A.: 1987, in V. E. Stepanov and V. N. Obridko (eds.), *Proceedings of Solar Max Analysis Conference*, VNU-Science Press, Irkutsk Meeting, p. 147.
Wiik, J .E., Heinzel, P., and Schmieder, B.: 1992, *Astron. Astrophys.* **260**, 419.